On the Use of a Zn/Mn-Based Material as Adsorbent at Room Temperature for Harmful H_2S Gas

Francisco José Alguacil , Manuel Alonso , José Ignacio Robla , Félix Antonio López *

Posted Date: 9 August 2023

doi: 10.20944/preprints202308.0791.v1

Keywords: hydrogen sulphide; adsorption; fixed-bed column; modelling; spent alkaline batteries; Zn-Mn-oxides mixture

Article

On the Use of a Zn/Mn-Based Material as Adsorbent at Room Temperature for Harmful H_2S Gas

Francisco José Alguacil, Manuel Alonso, José Ignacio Robla and Félix Antonio López *

Centro Nacional de Investigaciones Metalurgicas (CENIM-CSIC). Avda. Gregorio del Amo 8. 28040 Madrid, Spain; fjalgua@cenim.csic.es (F.J.A.); malonso@cenim.csic.es (M.A.); jrobla@cenim.csic.es (J.I.R.)

* Correspondence: f.lopez@csic.es

Abstract: Breakthrough curves for the adsorption of H2S using a metal-oxides mixture were predicted using the Bohart-Adams model of fixed bed adsorption. This mixture ($ZnMn_2O_4$+ZnO+Mn_2O_3) came from the processing of an urban waste as spent alkaline batteries were. The H2S adsorption experiments were carried out in a fixed-bed column at 20º C, and under various experimental conditions: gas flow rate, inlet H2S concentration and adsorbent dosage. Curves predicted by the model matched well with experimental data, providing data for the possible scale-up of the system. At the various experimental variables, the efficiency of the column, were also provided in the work. This investigation demonstrated the usefulness of a waste material, like spent alkaline batteries, to provide an adsorbent material to mitigate the problem of the presence of this harmful gas.

Keywords: hydrogen sulphide; adsorption; fixed-bed column; modelling; spent alkaline batteries; Zn-Mn-oxides mixture

1. Introduction

The presence of H_2S is an important issue due to its harmful effects on humans and the environment, but also to its corrosive character, the tending to poison catalysts, etc.; as a problem, it is of a particular interest is the presence of this H_2S in biogases. Both, wastes or anaerobic digestion, are responsible for biogas production, and it is currently used for domestic purposes in less developed countries around the world. Due to its high methane content (50%-70%), biogas is a clear substitute to natural gas in a series or practical applications including heat and electricity generation and biofuels. Thus, biogas production has incremented in Europe and other countries, and it is now considered of the utmost importance by the European Industrial Biomass Initiative (EIBI), the European Energy Research Alliance (EERA) or the Strategic Energy Plan (SET) plan.

Also, serious concerns on climate change and the less facile availability of oil and gas reserves (heavy escalated from 2022 by the Russian-Ukraine war), increased the interest of using biogas as a renewable substitute for natural gas. In fact, it is mentioned [1] about the possibility of scaling up renewable gas production between the beginning of 2020 decade and 2050 to more than 120 billion m3/year, this figure included both renewable hydrogen and biomethane. But this substitution presented problems, because some gases, as it is said above, including H_2S disturbed the usefulness of biogas, thus, its removal from biogas, and in general from gases streams, is of the utmost importance, being various the strategies proposed to reach this goal. Among them, H_2S adsorption on different materials is widely used, being some examples described in the very recent literature:

i) metal oxides adsorbents: pristine barium stannate and La^{3+} surface modified barium salt, various V_2O_5-based materials, zinc oxide particles [2–4],
ii) carbon derivatives (including biochars) adsorbents: MgFe2O4-loaded N-doped biochar (from cooked rice waste, activated carbon from petcoke, catalyst-loaded activated carbon, graphite slit nanopores, biochar supported Zn-Al-Fe layered double hydroxide, modified carbon nitride, Cu-impregnated activated carbon, dual chemical mixture or core–shell activated carbons [5–12],

 doi:10.20944/preprints202308.0791.v1

iii) zeolites-based adsorbents: Cu, Zn, Co, Mn-modified 13X zeolite, polyethylene glycol composites of 4A and Y zeolites or ETS-4 and ETS-10 titanosilicates, NaX and NaY zeolites, metallic-doped zeolitic imidazolate framework-8 coupled with microbiological desorption [13–16],
iv) biological-based adsorbents: purple phototrophic bacteria, urea-modified copper-based adsorbent [17,18],
v) nanostructural-based and fibres adsorbents: Cr, Ni, Al, C, Si, O, or S doped boron nitride nanotubes, activated waste jute nanoadsorbent, MIL-101(Cr)@UiO-66(Zr) nanocrystals, PMo12-modified waste rice husk fibres, Aminated polyacrylonitrile fibres [19–23],
vi) other adsorbent: titanium ilicalite-1/H_2O_2, [24] and iron oxide [25].

To contribute to these efforts to find suitable materials to remove H_2S from gas streams, the present work presents an investigation about the use of a metal oxides mixture ($ZnMn_2O_4$+ZnO+Mn_2O_3) as adsorbent of H_2S from a gas mixture of H_2S and N_2. The adsorbent is provided by the chemical treatment of an urban waste (spent alkaline and Zn/C batteries), and adsorption experiments are carried out in dynamic mode using a fixed bed column and under various experimental conditions: H_2S concentration, gas mixture flow and adsorbent dosage. Column parameters are derived under the various experimental conditions, as well as, the time required for the formation of the exchange zone and the time necessary to establish this exchange zone are calculated. A derived model predicted the breakthrough curves generated under the various experimental conditions, and also an equation to predict the column efficiency is developed in the work. Results show that this adsorbent can be used to clean a gas stream contaminated with harmful H_2S.

2. Materials and Methods

2.1 Modelling the Adsorption Process

The Bohart-Adams model of fixed bed adsorption [26] was used to model the H_2S adsorption onto the adsorbent. The model used two coupled first-order linear particle differential equations,

$$\frac{\partial a}{\partial t} = -kac \quad , \quad u\frac{\partial c}{\partial z} = -\rho_s kac \tag{1}$$

subjected to initial ($c = c_0$ at $z = 0$) and boundary ($a = a_0$ at $t = 0$) conditions.

In eq.(1), a (-) is the adsorption capacity of the bed (mass of H_2S that can be adsorbed per unit mass of solid), c (mass unit) is the solute concentration in the gas flow, k (volume/mass·time units) is the adsorption rate constant, ρ_s (mass/volume units) is the bed bulk density (mass of solid per unit volume of column units), u(length/time units) is the gas flow velocity, z (length unit) is the axial coordinate along the column, and t (time unit) represented the elapsed time.

At the initial condition, the H_2S concentration in the inlet gas stream is given, whereas at the boundary conditions, the adsorption capacity before the loading of H_2S onto the bed is given. Both formulations represented in eq.(1) are resolved as:

$$\frac{c}{c_0} = \frac{\exp(kc_0 t)}{\exp(kc_0 t) + \exp(ka_0\rho_s z/u) - 1} \tag{2a}$$

$$\frac{a}{a_0} = \frac{\exp(ka_0\rho_s z/u)}{\exp(kc_0 t) + \exp(ka_0\rho_s z/u) - 1}. \tag{2b}$$

Comparison of the above equations with the experimental breakthrough curve, are done at $z = H$, being H the height of the adsorbent packed in the column. Consideration of the gas flow rate, q (mass/time units), and the bed mass, m_s (mass units), allowed to write the next expression, which represented the model breakthrough curves:

Preprints (www.preprints.org) | NOT PEER-REVIEWED | Posted: 9 August 2023 doi:10.20944/preprints202308.0791.v1

$$\left(\frac{c}{c_0}\right)_{z=H} = \frac{\exp(kc_0 t)}{\exp(kc_0 t)+\exp(ka_0 m_s / q)-1}. \quad (3)$$

and k and a_0 values were determined, under the various experimental variables, by least square fitting of the experimental data to eq.(3). Fitting of the different operational conditions are represented in Figures 2–4. The use of this model represented H_2S loading onto this $ZnMn_2O_4$+ZnO-based adsorbent in an adequate form.

2.2. Characterization Techniques

X-ray diffraction (XRD, D8 Advance, Bruker AXS GmbH, Germany) analyses were performed with copper anode (CuKα1 λ = 0.15418 nm) working at 40 kV and 40 mA. Determinations were done on samples rotating at 15 rpm in the interval 10–70° (2θ) and X-ray patterns were acquired with a step/size of 0.02° and time/step of 2s.

The chemical analysis was carried out by means of wavelength dispersion using a X-ray Fluorescence (XRF) technique in a PANalytical equipment (MagicX PW-2424, Philips, The Netherlands) with a Rh anode RX tube (SUPER SHARP) and generator. 2.4 KW.

The chemical composition and elemental spatial distribution were assessed by energy dispersive X-ray microanalysis (EDX, Bruker Quantax) in a Leica 440 Steroscan SEM.

3. Results

3.1. Synthesis of Adsorbent

The adsorbent synthesis was performed following the procedure described in the literature [27]. The resulting material (black mass) from spent alkaline or Zn/C batteries was treated in several steps comprising electrolyte removal, oxidative leaching and selective two-step precipitation. The final product of these steps was a mixture of $ZnMn_2O_4$, ZnO and Mn_2O_3 This mixture was used as adsorbent for H_2S. The chemical composition of the oxides mixture is shown in Table 1.

Table 1. Chemical composition of the adsorbent.

Element	Mn	Zn	K	Fe	Na	Ni	Al
Wt,%	38.80	29.70	3.30	0.48	0.15	0.46	0.06

As it was expected, manganese and zinc formed the predominant species in the material. From the results of the XRD characterization of the oxides mixture (not shown in this article), the phases were quantified by Rietveld refinement. The results are shown in Table 2. These spinel based compounds have crystal sizes in the range of 50-100nm [28].

Table 2. Mineralogical composition of the oxides mixture.

Compound Name	Chemical Formula	Concentration (%)
Zinc Oxide	ZnO	16.2
Zinc Manganese Oxide	$ZnMn_2O_4$	56.4
Hausmannite	Mn_3O_4	26.8
Zinc Manganese Oxide Hydrate	$ZnMn_3O_7(H_2O)_3$	0.7

3.2. Dynamic Adsorption Tests

Figure 1 shows the experimental set up designed and installed for the H_2S adsorption determination on to the investigated material. The test was developed at room temperature (20º C). The weighed adsorbent sample is contained in a column. The gas test mixture flows upside down, and the relative proportions of H_2S and the carrier gas (N_2) (from separated bottles) was controlled by Bronk Horst HI-TEC F-201C-FA-22-V mass flow controller in the case of H_2S and by Alicat

Preprints (www.preprints.org) | NOT PEER-REVIEWED | Posted: 9 August 2023 doi:10.20944/preprints202308.0791.v1

Scientific MC-500SCCM-D mass flow controller for N_2. The flow range varied between 0 and 200 mL/min in the case of the H_2S controller and between 0 and 500 mL/min in the case of the N_2 controller. An Amphenol SGX Sensortech 4 series electrochemical gas sensor was used for online determination of the H_2S concentration exiting the column. Data was stored using a data acquisition computer running specific software (SGX ECVQ-EK3 Gas Sensor Evaluation KIT V 2.1.0). With the same computer the mass-flow controller parameters are established.

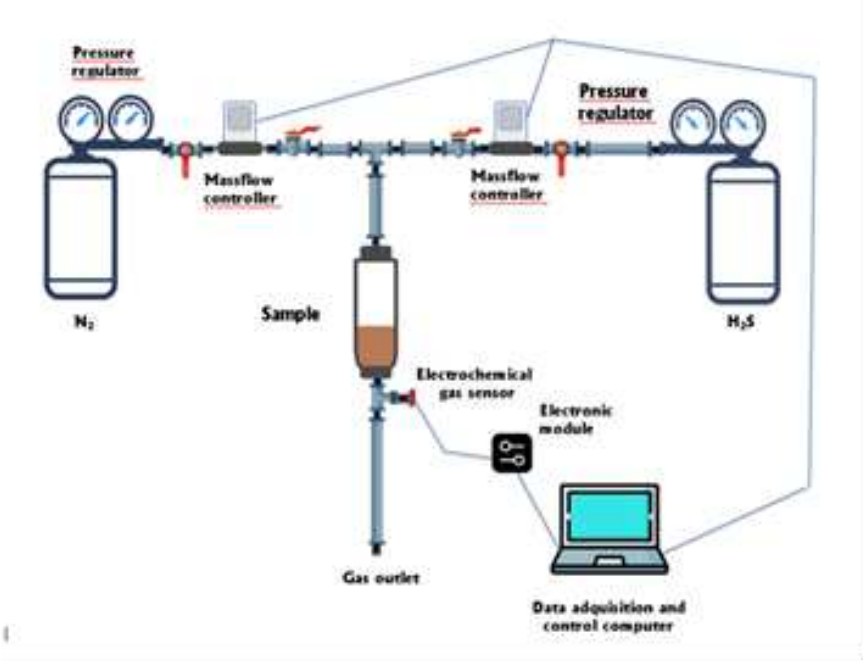

Figure 1. Schematic view of the set up used to investigate H_2S uptake onto the adsorbent.

In the present work, the breakthrough point or time is estimated at the time in which the next relation is equal to 0.051:

$$\frac{[H_2S]_{out}}{[H_2S]_{in}} \quad (4)$$

where $[H_2S]_{out}$ and $[H_2S]_{in}$ are the H_2S concentrations exiting and feeding the column, respectively.

3.3. Column Parameters

These parameters were calculated according to the next formulation [29]:

$$D_w \frac{V_{0.5} - V_d - V_i}{W_a} \quad (5)$$

where D_w was the weight distribution coefficient, $V_{0.5}$ was the volume of gas exiting the column at $[H_2]_{out}/[H_2S]= 0.5$, V_d was the dead column volume, V_p the intergranular volume and W_d the adsorbent mass packed in the column.

$$D_b = D_w \cdot d_a \quad (6)$$

where D_b represented the bed distribution coefficient and d_a was the adsorbent density.

$$C_{ep} = \frac{V_{ep} \cdot [H_2S]_{in}}{V_a} \quad (7)$$

where C_{ep} was the capacity at the end point $[H_2S]_{out}/[H_2S]_{in}= 0.95$, V_{ep} was the gas volume exiting the column at this same point, and V_a was the volume of adsorbent in the column.

Preprints (www.preprints.org) | NOT PEER-REVIEWED | Posted: 9 August 2023 doi:10.20944/preprints202308.0791.v1

$$C_{ep-bp} = \frac{(V_{ep} - V_{bp})[H_2S]_{in}}{V_a} \quad (8)$$

in the above equation, C_{ep-bp} was the capacity from the breakthrough point to the end point and V_{bp} was the exiting gas volume to the breakthrough point.

Equations (9) and (10) were used to calculate the time necessary for the formation of the adsorption zone (t_{az}) and the time at which the adsorption zone was established (t_{ae}), respectively:

$$t_{az} = \frac{V_{ep} - V_{bp}}{Q} \quad (9)$$

$$t_{ae} = \frac{V_{ep}}{Q} \quad (10)$$

where Q was the gas flow.

4. Results and Discussion

Prior to a practical application of a given adsorption system, it is of a necessity to investigate the H_2S performance of the adsorptive material under various experimental operational conditions. Thus, in order to further investigate the potential of this oxides mixture, various experimental parameters were considered to investigate their influence on the performance of the present adsorbent.

4.1. Influence of the Inlet H_2S Concentration

The removal of H_2S from the gas stream was investigated in a fixed-bed column at 20º C. Figure 2 showed the influence of H_2S concentration entering the column on H_2S adsorption. The figure showed that the H_2S capture ability of the adsorbent material depended on the inlet H_2S concentration; it can be seen, that the greater the inlet concentration was, the shorter the breakthrough time. It was also shown in the Figure, that the slope of the curves became fairly similar, and the period time between the breakthrough time and the time in which the adsorbent was completely loaded by the gas increased due to increase in the inlet H_2S dosage. Apparently, the H_2S concentration entering the column and the H_2S concentration exiting the column at the breakthrough point presented any relationship.

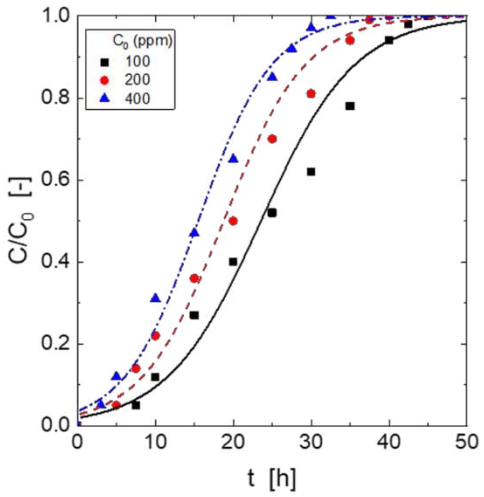

Figure 2. Breakthrough curves at various inlet H_2S concentrations. (Adsorbent dosage: 2 g. Inlet gas flow: 220 cm^3/min. Experimental data (points). Model data (lines)).

These results were attributable to that the similarity in the slopes yielded using the different H_2S concentrations entering the fixed bed, and to that an increase in this H_2S concentration produced and

Preprints (www.preprints.org) | NOT PEER-REVIEWED | Posted: 9 August 2023 doi:10.20944/preprints202308.0791.v1

increase in the period time comprised between the breakthrough point and the point in which the bed is considered to be loaded with the gas ($[H_2S]_{out}/[H_2S]_{in} = 0.95$).

The above results to that the increase of the H_2S concentration entering the column produced a longer mass transfer zone in the packed bed. For the greatest inlet concentration gas phase, the breakthrough time was 3 hours, whereas for the lowest concentration the breakthrough time was extended to 7.5 hours. Table 3 showed typical breakthrough capacities, when the inlet H_2S concentration was 400 mg, the H_2S breakthrough capacity of the adsorbent material was 7.9 g/g. A H_2S capture of 5.0 g/g can be reached when the inlet gas concentration was 100 mg.

Table 3. Influence of inlet H_2S concentration on breakthrough capacity (Adsorbent dosage: 2 g. Inlet gas flow: 220 cm^3/min).

Inlet H_2S concentration (mg)	Breakthrough capacity g/g	K (L/g·h)	a_0 (g/g)	r^2
100	5.0	1.66	15.6	0.9555
200	6.6	0.95	25.0	0.9501
400	7.9	0.53	41.4	0.9813

The gas stream volumes exiting the column to the breakthrough point were 99 L for 100 mg H_2S, 66 L for 200 mg H_2S and near 40 L for an initial H_2S concentration of 400 mg. Considering these exiting volumes and the order of occurrence of each plot in Figure 3, it can be observed that lowest H_2S concentration produced the larger volume of clean gas.

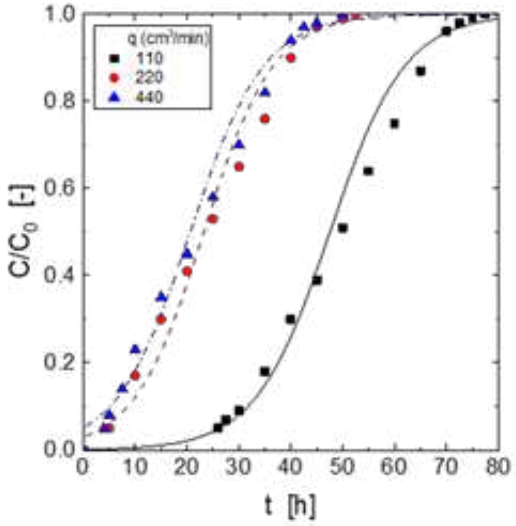

Figure 3. Breakthrough curves at various inlet gas flows. (Adsorbent dosage: 4g. Inlet H_2S concentration: 400 mg. Experimental data: points Model data (lines)).

When the concentration of the pollutant in the gas stream is the highest (400 mg), the quickest the column was saturated. The total volume to the exhaustion point was near 548 L and 383 L for inlet H_2S concentrations of 100 and 400 mg, respectively.

Using eqs. (5-10), the column parameters at the various inlet H_2S concentrations were calculate and summarized in Table 4. Also, times required for the formation and establishment of the adsorption zone were showed in this same Table. It can be observed, the increase of the toxic gas concentration feeding the column produced an increase of both types of capacities, whereas the times associated with this adsorption were longer with the lowest H_2S inlet concentration.

Preprints (www.preprints.org) | NOT PEER-REVIEWED | Posted: 9 August 2023 doi:10.20944/preprints202308.0791.v1

Table 4. Column parameters at the various inlet H_2S concentrations.

$[H_2S]_{in}$	D_w (L/g)	D_b	C_{ep} (g/L)	C_{ep-bp} (g/L)	t_{az} (h)	t_{ae} (h)
100	158	>600000	29	24	34	42
200	132	>500000	49	42	30	35
400	99	>400000	81	72	26	29

4.2. Influence of the Gas Mixture Flow

Figure 3 showed the breakthrough curves at various gas flow rates, whereas its corresponding breakthrough capacities was shown in Table 5. From Figure 3, it can be seen that the increase of the gas flow rate decreased the time to reach the breakthrough point. Lower gas flow resulted in longer times to reach the breakthrough point, and the loading curve presented a smoother shape; less pronounced breakthrough curves may be an indication of lower H_2S loading onto the adsorbent, however, these results indicated against the above. According with the literature [30], the breakthrough curves were pictures of the phenomena occurring in the mass transfer zone of the bed. A non-reversal adsorption process, similarly to that of the present study using metal oxides mixture-based beds, and before the breakthrough point, there was always unused adsorbent to evolve a mass transfer zone ready to react with the gas stream entering the column. Thus, the gas exiting the bed remained undetected, being the rate at which the adsorption occurred, the overall rate corresponding to the mass transfer zone. The displacement of the mass transfer zone towards the bed bottom produced that there was not more available unused adsorbent to react with the gas entering the column, and unreacting H_2S exits the column. If one considered an infinite overall reaction rate, the mass transfer zone occurred in a thin layer of adsorbent, and the H_2S concentration exiting the column equalled the inlet value in a very short time. In this condition, the breakthrough curves adopted an ideal vertical shape when $[H_2S]_{out}/[H_2S]_{in}$ was represented against time.

Table 5. Influence of gas flow on breakthrough capacity (Adsorbent dosage: 4g. Inlet H_2S concentration: 400 mg).

Gas flow (cm^3/min)	Breakthrough capacity (g/g)	K (L/g·h)	a_0 (g/g)	r^2
110	17.2	0.35	31.4	0.9739
220	6.6	0.37	30.9	0.9706
440	11.9	0.35	55.4	0.9639

However, this situation was uncommon because in the mass transfer zone the corresponding reaction rate occurred to be finite, thus, the slower the overall reaction rate in the mass transfer zone the lesser the step shape of the curves. Figure 4 showed that a greater reaction rate was accompanied by a greater flow rate, the above being attributable to that mass transfer regime controlled the process.

Table 5 resumed the quantitative results of the above series of experiments. At a flow rate of 110 cm^3/min, the H_2S removal capacity was 17.2 g/g. With an increase of the flow rate to 220 cm^3/min, H_2S uptake decreased to near 7 g/g. These results indicated that this Zn-Mn-oxides mixture was best suitable for H_2S removal from a gas stream using low flow rates, with the best capacity ability, under the present experimental conditions, of 17.2 g/g.

Preprints (www.preprints.org) | NOT PEER-REVIEWED | Posted: 9 August 2023 doi:10.20944/preprints202308.0791.v1

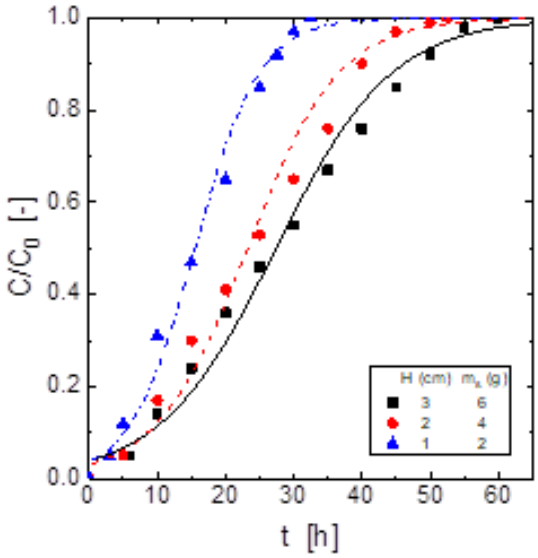

Figure 4. Breakthrough curves at various adsorbent dosages. (Inlet H_2S concentration: 400 mg. Inlet gas flow: 220 cm^3/min. Experimental data (points). Model data (lines)).

Table 6 showed the column parameters calculated for the various flow rates investigated in the present work. The increase of the flow rate produced an increase of both solute uptakes at the exhaustion point and from the breakthrough point to the exhaustion point. Also, the time necessary for the formation and the establishment of the adsorption zone increased with the decrease of the gas flow rate feeding the column

Table 6. Column parameters at the various flow rates.

Gas flow (cm^3/min)	D_w (L/g)	D_b	C_{ep} (g/L)	C_{ep-bp} (g/L)	t_{az} (h)	t_{ae} (h)
110	81	>300000	48	30	43	69
220	79	>300000	63	56	40	45
440	143	>600000	111	99	36	40

4.3. Influence of the Adsorbent Dosage

In order to investigate in-depth influence of the adsorbent dosage on the H_2S removal process, this work performed H_2S adsorption tests at adsorbent dosages of (2, 4 and 6 g). Figure 4 showed that when the adsorbent dosage was increased, the adsorbent material showed a greater H_2S adsorptive ability in terms of reaching the breakthrough point at more extended period time. However, the greatest adsorption capacity was yielded using the lowest adsorbent dosage (Table 7). The load of H_2S on this material was connected to the moving boundary model, and the mass transfer across the adsorbent shell particle dominated, as a consequence, an increase in the thickness of the shell produced a decrease in the adsorption rate of the gas.

Table 7. Influence of adsorbent dosage on breakthrough capacity.

Adsorbent dosage (g)	Breakthrough capacity (g/g)	K (L/g·h)	a_0 (g/g)	r^2
2	7.9	0.53	41.4	0.9813
4	6.6	0.37	30.9	0.9706
6	5.3	0.29	24.4	0.9699

(Inlet H_2S concentration: 400 mg. Inlet gas flow: 220 cm^3/min).

 doi:10.20944/preprints202308.0791.v1

The variation of the adsorbent dosage packed into the column resulted in a variation of the volume of the gas exiting the column to the breakthrough point, thus, using 2 g of the adsorbent, this volume was of 40 L of clean gas, whereas with a dosage of 6 g, the corresponding volume was of 79 L. That is, the increase of the adsorbent dosage resulted in an increase of the volume of clean gas exiting the column.

As Figures 2–4 showed, the breakthrough curves followed the S-shape profile, which was common of most of the cases of adsorption processes by column operational methodology. Whereas in Figures 3–5 fitting of eq.(3) to the various experimental conditions were shown as continuous lines, Tables 2, 4 and 6 showed k and a_0 values resulting from these fitting. Within the model used in this work, H_2S loading onto this $ZnMn_2O_4$+ZnO+ Mn_2O_3-based adsorbent is well represented.

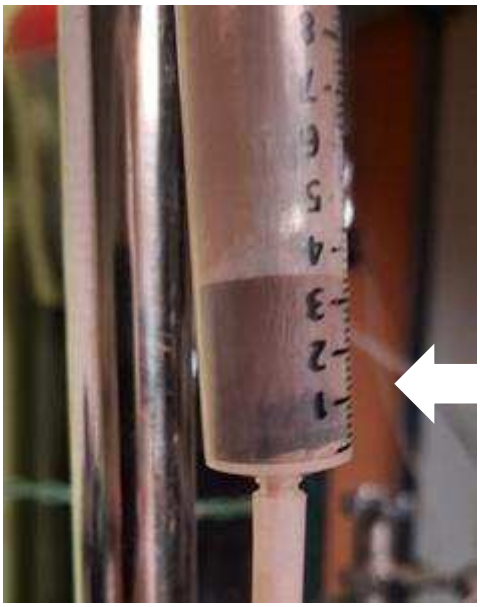

Figure 5. Aspect of the H_2S loaded adsorbent (upper part) and unloaded adsorbent (bottom part).

Under the various experimental conditions, the adsorbent material showed similar adsorption behaviour. It can initially adsorb H_2S efficiently in order to maintain H_2S concentration in the gas stream exiting the column to meet the purification level ($[H_2S]_{out}/[H_2S]_{in}<0.051$), and then breakthrough occurs in a very short time, which can be attributed to a fast reaction kinetics of gas adsorption by the adsorbent material [7,31].

Adsorption of H_2S on the metal oxides mixture causes a colour change of the adsorbent from dark brown to light brown (Figure 5), this change of colour is observed in the upper part of the adsorbent bed.

Figure 6a shows the EDX spectrum of the oxide mixture before the adsorption process. Figure 6b shows the EDX spectrum of the product resulting from the adsorption process. A clear peak corresponding to S kα is observed, which can be attributed to MnS, as can be seen in Figure 6c, which shows the RX diffraction pattern of the product obtained after adsorption. The presence of zinc sulphides was not observed (probably because it was also in amorphous form), in any case, the formation of metal-sulphide-species, as a result of the process of the loading of H_2S onto the adsorbent, was demonstrated.

Preprints (www.preprints.org) | NOT PEER-REVIEWED | Posted: 9 August 2023 doi:10.20944/preprints202308.0791.v1

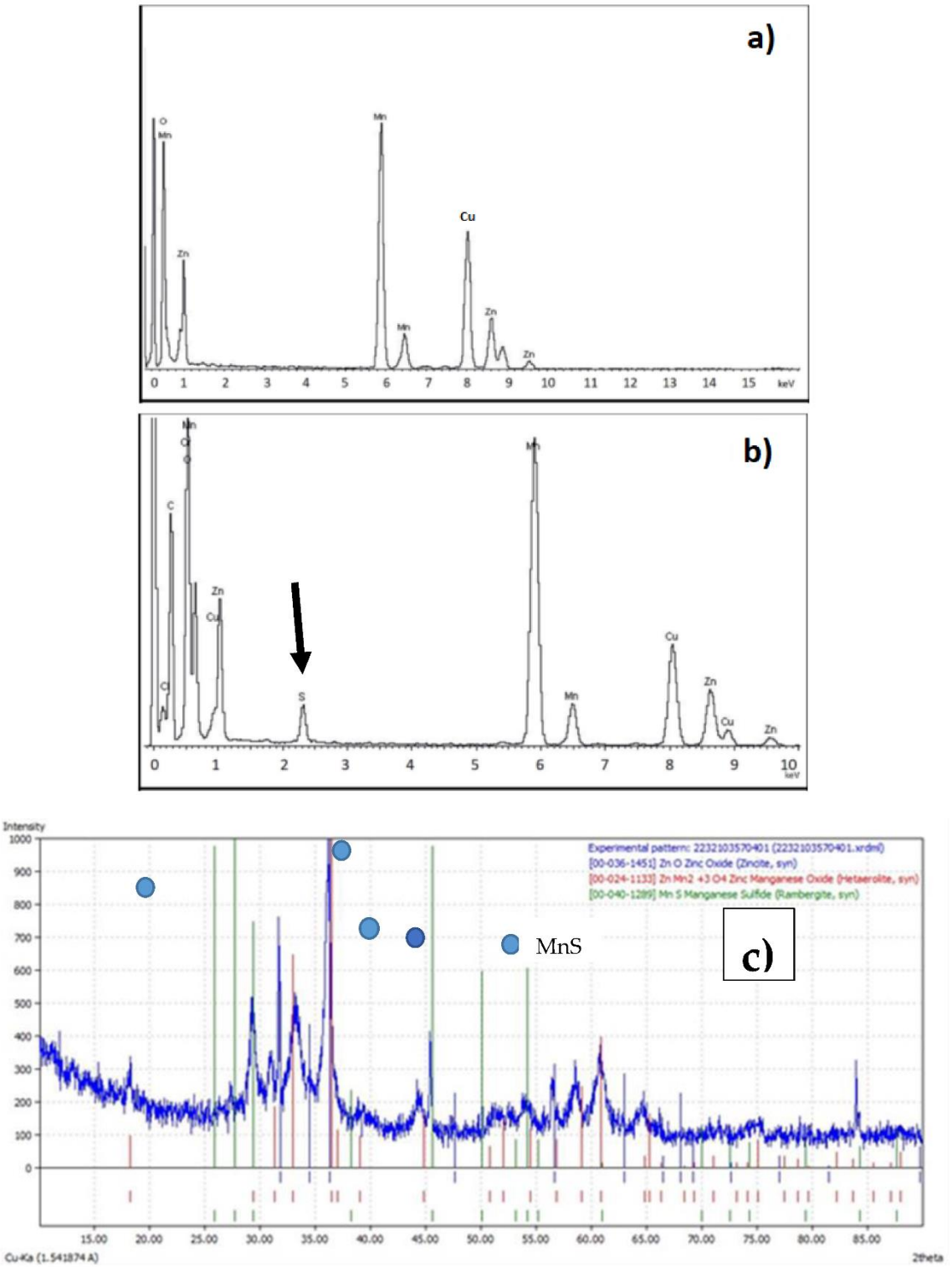

Figure 6. EDX spectrum of (**a**) initial metal oxides, (**b**) metal oxides after adsorption and (**c**) XRD pattern of metal oxides after being loaded with H_2S.

4.4. Estimation of Fixed-Bed Efficiencies

The adsorption efficiency of the packed adsorbent can be calculated:
i) instantaneously with respect of time:

$$E_{ins}\left((t)\right) = 1 - \frac{c_t}{c_0} \tag{11}$$

Preprints (www.preprints.org) | NOT PEER-REVIEWED | Posted: 9 August 2023 doi:10.20944/preprints202308.0791.v1

or ii) averagely over a time t:

$$E(t) = \frac{1}{t}\int_0^t \left(1 - \frac{c}{c_0}\right) dt \tag{12}$$

Insertion of eq. (2a) in eq.(12), allowed to derive the next equation:

$$E(t)) = 1 - \frac{1}{kc_0 t} \ln \frac{\exp(kc_0 t) + \exp(ka_0 m_s / q) - 1}{\exp(ka_0 m_s / q)} \tag{13}$$

Fitting of experimental data to eq.(13) (Figure 7), showed that this last expression predicted in a reasonable form the column efficiencies at the different experimental conditions used in this investigation.

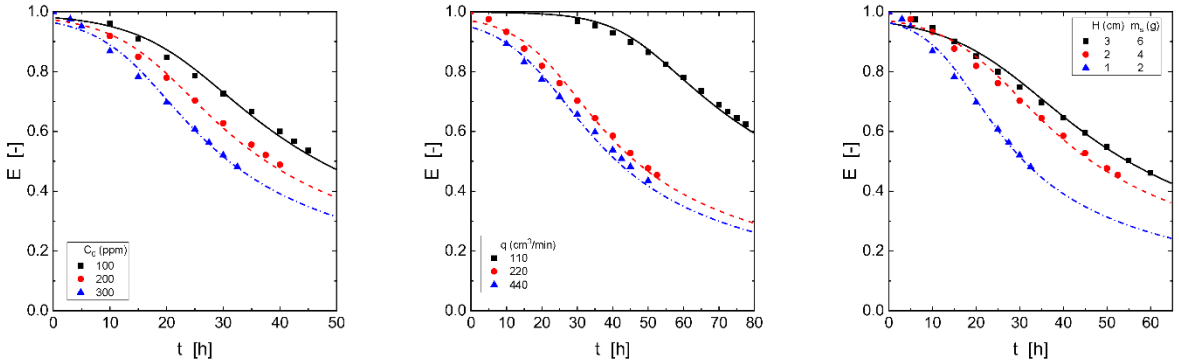

Figure 7. Experimental (symbols) and model (eq. (13) (lines) column efficiencies. Upper left figure: Influence of H_2S concentration. Upper right figure: Influence of the gas mixture flow. Bottom figure: Influence of the adsorbent dosage.

5. Conclusions

The use of $ZnMn_2O_4$+ZnO+Mn_2O_3 mixture, coming from urban wastes, to clean mimic biogas (H_2S+N_2) is demonstrated. The adsorption of harmful H_2S onto the adsorbent is dependent on different experimental variables, such as H_2S concentration in the gas mixture, gas mixture flow, and adsorbent dosage. The breakthrough point increases as the H2S dosage decreased from 400 mg to 100 mg, the gas mixture flow decreased from 440 cm^3/min to 110 cm^3/min, and when the adsorbent dosage increased from 2g to 6 g.

Column parameters varies according with the results mentioned above, i.e. capacity to the exhausted point increased with the increase of the H_2S concentration in the gas, the increase of the gas flow and the decrease of the adsorbent dosage packed in the column.

There is a reasonable certainty that upon H_2S uptake onto the adsorbent, metal oxides species present in the solid material evolved to metal sulphides species.

The model used, with the corresponding model parameters properly identified, allowed to a good prediction of the experimentally determined breakthrough curves. Also, column efficiencies can be estimated by means of an equation, which used the experimental results obtained under the different experimental variables considered in this work.

Author Contributions: F.J.A.: conceived and designed the experiment, wrote the manuscript, and supervised the work. M.Á.A.: derived the models from the experimental data and wrote the manuscript. F.A.L.: synthesis and characterized the adsorbent and wrote the manuscript. J.I.R.: conceived and designed the experiment and wrote the manuscript. All authors have read and agreed to the published version of the manuscript.

Funding: This work was supported by the GONDOLA project from the Agencia Española de Investigación (AEI), agreement No. PDC2021-120-799-I00

Data Availability Statement: Not applicable.

Acknowledgments: The authors belong to the CSIC Interdisciplinary Thematic Platform PTI-TRANSENER+

Conflicts of Interest: The authors declare no conflict of interest.

References

1. S.Alberici , G.Toop, W.G. Biomethane production potentials in the EU Available online: https://gasforclimate2050.eu/wp-content/uploads/2022/10/Guidehouse_GfC_report_design_final_v3.pdf (accessed on Aug 8, 2023).
2. Marikutsa, A.; Dobrovolskii, A.A.; Rumyantseva, M.N.; Mikhaylov, A.A.; Medvedev, A.G.; Lev, O.; Prikhodchenko, P. V Improved H2S sensitivity of nanosized BaSnO3 obtained by hydrogen peroxide assisted sol-gel processing. *J. Alloys Compd.* **2023**, *944*, 169141, doi:https://doi.org/10.1016/j.jallcom.2023.169141.
3. Chen, L.; Ma, J.; Peng, J.; Song, T.; Liu, K. Effect of CuO addition on the performance of V2O5-based oxygen carriers for chemical-looping oxidation of H2S for efficient sulfur recovery from natural gas. *Fuel* **2023**, *337*, 126898, doi:https://doi.org/10.1016/j.fuel.2022.126898.
4. Ciro, E.; Dell'Era, A.; Hatunoglu, A.; Bocci, E.; Del Zotto, L. Kinetic and Thermodynamic Study of the Wet Desulfurization Reaction of ZnO Sorbents at High Temperatures. *Energies* 2023, *16*.
5. Yuan, Y.; Huang, L.; Yılmaz, M.; Zhang, T.C.; Wang, Y.; Yuan, S. MgFe2O4-loaded N-doped biochar derived from waste cooked rice for efficient low-temperature desulfurization of H2S. *Fuel* **2023**, *339*, 127385, doi:10.1016/j.fuel.2022.127385.
6. Jacobs, J.H.; Chou, N.; McKelvie, K.H.; Commodore, J.A.; Sui, R.; Lesage, K.L.; Wynnyk, K.G.; Xiao, Y.; Biesinger, M.C.; Hill, J.M.; et al. Screening activated carbons produced from recycled petroleum coke for acid gas separation. *Carbon Trends* **2023**, *10*, 100243, doi:10.1016/j.cartre.2022.100243.
7. Liu, B.; Zuo, S. Effect of Catalytic Factors of Activated Carbon and Gas Stream Properties on H2S Catalytic Conversion. *Water, Air, Soil Pollut.* **2023**, *234*, 118, doi:10.1007/s11270-023-06141-x.
8. Kuo, J.-K.; Tsai, Y.-T.; Huang, P.-H.; Lee, C.-H.; Lin, C.-H. Adsorption and purification of biogas inside graphitic nanopores: molecular dynamics simulation approach. *J. Mol. Model.* **2023**, *29*, 40, doi:10.1007/s00894-023-05450-6.
9. Kong, F.; Xie, Y.; Xia, C.; Huang, H.; Liang, D.; Qiu, Y.; Zhang, Q.; Liu, X.; Shao, H.; Meng, Z. Removal of hydrogen sulfide by layered double hydroxide loaded biochar in dynamic adsorption experiment. *Surfaces and Interfaces* **2023**, *36*, 102487, doi:10.1016/j.surfin.2022.102487.
10. Tabarkhoon, F.; Abolghasemi, H.; Rashidi, A.; Bazmi, M.; Alivand, M.S.; Tabarkhoon, F.; Farahani, M.V.; Esrafili, M.D. Synthesis of novel and tunable Micro-Mesoporous carbon nitrides for Ultra-High CO2 and H2S capture. *Chem. Eng. J.* **2023**, *456*, 140973, doi:10.1016/j.cej.2022.140973.
11. Ko, K.-J.; Kim, H.; Cho, Y.-H.; Kim, K.-M.; Lee, C.-H. Desulfurization of ultra-low-concentration H2S in natural gas on Cu-impregnated activated carbon: Characteristics and mechanisms. *Sep. Purif. Technol.* **2023**, *305*, 122539, doi:10.1016/j.seppur.2022.122539.
12. Zulkefli, N.N.; Noor Azam, A.M.I.; Masdar, M.S.; Isahak, W.N.R.W. Adsorption–Desorption Behavior of Hydrogen Sulfide Capture on a Modified Activated Carbon Surface. *Materials (Basel).* **2023**, *16*, 462, doi:10.3390/ma16010462.
13. Guo, Y.; Xiang, B.; Zhao, B.; Wang, W.; Xiang, Y.; Liao, J.; Chang, L.; Ma, J.; Bao, W. Removal of H2S from simulated blast furnace gas by adsorption over metal-modified 13X zeolite. *Fuel* **2023**, *338*, 127261, doi:10.1016/j.fuel.2022.127261.
14. Carvalho, S.; Pinto, R. V.; Pires, J.; Rocha, J.; Antunes, F.; Pinto, M.L. Evaluation of the H2S and NO adsorption and release capacity of PEG-zeolites and PEG-titanosilicates composites. *Microporous Mesoporous Mater.* **2023**, *350*, 112432, doi:10.1016/j.micromeso.2023.112432.
15. Pereira, M. V.; de Oliveira, L.H.; do Nascimento, J.F.; Arroyo, P.A. Simulation of high-pressure sour natural gas adsorption equilibrium on NaX and NaY zeolites using the multicomponent potential theory of adsorption. *Adsorption* **2023**, *29*, 65–72, doi:10.1007/s10450-022-00373-9.
16. Ahmad, M.; Yousaf, M.; Cai, W.; Zhao, Z.-P. Enhanced H2S removal from diverse fuels by a coupled absorption and biological process uses CO2 as carbon resource for microbial ecosystem. *Sep. Purif. Technol.* **2023**, *310*, 123182, doi:10.1016/j.seppur.2023.123182.
17. Egger, F.; Hülsen, T.; Batstone, D.J. Continuous H2S removal from biogas using purple phototrophic bacteria. *Chem. Eng. J.* **2023**, *454*, 140449, doi:10.1016/j.cej.2022.140449.
18. Feng, J.; Jia, L.; Wang, F.; Sun, X.; Ning, P.; Wang, C.; Li, Y.; Li, K. Urea-modified Cu-based materials: Highly efficient and support-free adsorbents for removal of H2S in an anaerobic and dry environment. *Chem. Eng.*

J. **2023**, *451*, 138815, doi:10.1016/j.cej.2022.138815.

19. Yadav, A. Insights on the enhanced hydrogen sulfide adsorption on X (X = Cr, Ni, Al, C, Si, O, S) doped boron nitride nanotubes. *Comput. Theor. Chem.* **2023**, *1220*, 114005, doi:10.1016/j.comptc.2022.114005.
20. Liu, Z.; Qiu, K.; Sun, G.; Ma, Y.; Wang, Y.; Peng, J.; Chen, S.; Song, X. Aminated polyacrylonitrile fibers for the removal of hydrogen sulfide from natural gas at room temperature. *Res. Chem. Intermed.* **2023**, *49*, 701–716, doi:10.1007/s11164-022-04897-1.
21. Huang, Y.; Wang, J.; Ma, S.; Wang, R.; Wang, Y. Enhanced adsorption-oxidation performance of PMo12 immobilized onto porous MCM-41 derived from rice husk for H2S at room temperature. *Fuel* **2023**, *333*, 126448, doi:10.1016/j.fuel.2022.126448.
22. Ahmadi, R.; Ardjmand, M.; Rashidi, A.; Rafizadeh, M. Enhanced gas adsorption using an effective nanoadsorbent with high surface area based on waste jute as cellulose fiber. *Biomass Convers. Biorefinery* **2023**, *13*, 3071–3086, doi:10.1007/s13399-021-01370-8.
23. Fakhraie, S.; Rajabi, H.R.; Rashidi, A. Fabrication and application of novel core–shell MIL-101(Cr)@UiO-66(Zr) nanocrystals for highly selective separation of H2S and CO2. *Chem. Eng. J.* **2023**, *452*, 139001, doi:10.1016/j.cej.2022.139001.
24. Wang, Q.; Chen, Y.; Chen, Y.; Chen, D.; Tian, X.; Zhou, J.; Li, X.; Wang, Y. Removal of Gaseous H 2 S by the Titanium Silicalite-1/H 2 O 2 Wet Oxidation System. *Energy & Fuels* **2023**, *37*, 1169–1179, doi:10.1021/acs.energyfuels.2c03067.
25. Alguacil, F.J.; Alonso, M.Á.; López, F.A.; Robla, J.I. Dynamic Adsorption of H2S onto a Goethite-Based Material. *Molecules* **2022**, *27*, 7983, doi:10.3390/molecules27227983.
26. Bohart, G.S.; Adams, E.Q. Some aspects of the behaviour of charcola with respect to chlorine. *J. Am. Chem. Soc.* **1920**, *42*, 523–544, doi:10.1021/ja01448a018.
27. Romo, L.A.; López-Fernández, A.; García-Díaz, I.; Fernández, P.; Urbieta, A.; López, F.A. From spent alkaline batteries to Zn x Mn 3−x O 4 by a hydrometallurgical route: synthesis and characterization. *RSC Adv.* **2018**, *8*, 33496–33505, doi:10.1039/C8RA06789A.
28. Maroño, M.; Ortiz, I.; Sánchez, J.M.; Alcaraz, L.; Alguacil, F.J.; López, F.A. Effective removal of hydrogen sulfide using Mn-based recovered oxides from recycled batteries. *Chem. Eng. J.* **2021**, *419*, 129669, doi:10.1016/j.cej.2021.129669.
29. Wołowicz, A.; Staszak, K.; Hubicki, Z. Removal of Copper(II) in the Presence of Sodium Dodecylobenzene Sulfonate from Acidic Effluents Using Adsorption on Ion Exchangers and Micellar-Enhanced Ultrafiltration Methods. *Molecules* **2022**, *27*, 2430, doi:10.3390/molecules27082430.
30. Adanez, J.; Abad, A.; García-Labiano, F.; De Diego, L.; Gayán, P. HS retention with Ca-based sorbents in a pressurized fixed-bed reactor: application to moving-bed design. *Fuel* **2005**, *84*, 533–542, doi:10.1016/j.fuel.2004.10.004.
31. Yang, C.; Florent, M.; de Falco, G.; Fan, H.; Bandosz, T.J. ZnFe2O4/activated carbon as a regenerable adsorbent for catalytic removal of H2S from air at room temperature. *Chem. Eng. J.* **2020**, *394*, 124906, doi:10.1016/j.cej.2020.124906.